ROBUST BAYESIAN RECONSTRUCTION OF MULTISPECTRAL SINGLE-PHOTON 3D LIDAR DATA WITH NON-UNIFORM BACKGROUND

Abderrahim Halimi[1], *Jakeoung Koo*[1], *Robert A. Lamb*[2], *Gerald S. Buller*[1], *Stephen McLaughlin*[1]

(1) School of Engineering and Physical Sciences, Heriot-Watt University, Edinburgh U.K.
(2) Leonardo MW Ltd, Crewe Road North, Edinburgh, EH5 2XS, UK

ABSTRACT

This paper presents a new Bayesian algorithm for the robust reconstruction of multispectral single-photon Lidar data acquired in extreme conditions. We focus on imaging through obscurants (i.e., fog, water) leading to high and possibly non-uniform background noise. The proposed hierarchical Bayesian method accounts for multiscale information to provide distribution estimates for the target's depth and reflectivity, i.e., point and uncertainty measures of the estimates to improve decision making. The correlations between variables are enforced using a weighting scheme that allows the incorporation of guide information available from other sensors or state-of-the-art algorithms. Results on synthetic and real data show improved reconstruction of the scene in extreme conditions when compared to the state-of-the-art algorithms.

Index Terms— 3D reconstruction, multispectral Lidar imaging, obscurants, Bayesian inference, robust estimation.

1. INTRODUCTION

Single-photon 3D Lidar imaging is a promising technology due to the use of highly sensitive single-photon detectors that have excellent surface-to-surface resolution due to their picosecond timing performance [1, 2]. This sensor illuminates the scene with picosecond duration laser pulses and collects the reflected photons together with their time of flight (ToF), to build histograms of counts with respect to (w.r.t.) ToFs. The target's depth and reflectivity information could be extracted from these histograms, providing a 3D reconstruction of the observed scene. Moreover, a multispectral reconstruction of the scene could be obtained by using multiple laser wavelengths. Current challenges of 3D Lidar imaging includes the sparse photon nature of the target returns due to rapid or long-range imaging [3–7], in addition to high and possibly non-uniform background noise when imaging through obscurants [1, 8–12] (i.e., fog, water, smoke) as required in real-world applications (e.g., autonomous navigation, firefighting).

Several solutions have been proposed in the literature which can be grouped into three categories: statistical, learning-based and hybrid methods. The former presents good interpretability as they build on principled statistical models, but they require the definition of good features to represent the data [13–17]. Learning methods learn features/correlations from data, but often require large training datasets and can be sensitive to mismodeling effects [18–21]. Hybrid methods combine the two approaches to improve performance [22, 23] and an increasing effort is now devoted to improve interpretability of these methods [24, 25].

This paper proposes a robust statistical Bayesian algorithm designed to enable multispectral 3D imaging through obscurants in presence of non-uniform background. The method accounts for the Poisson data statistics, and improves inference performance by exploiting multiscale information on data and prior knowledge on depth and reflectivity parameters. The method also accounts for side information coming from other sensors and/or state-of-the-art algorithms by considering weight coefficients, that enforce structural data correlations. The resulting posterior distribution provides rich information about the parameters, i.e., point estimates and a measure of their variances. The model is designed to allow independent parameter updates, which enables fast inference. To summarize, the main contributions are the robustness to non-uniform background, quantified uncertainty of the parameters and a formulation exploiting guiding information from other algorithms/sensors. The benefit of these contributions is highlighted on synthetic and real data when compared to state-of-the-art algorithms.

The paper is structured as follows. Section 2 introduces the considered approximate likelihood and multiscale observation model. Section 3 presents the proposed hierarchical Bayesian model. Results on simulated and real data are presented in Sections 4 and 5. Conclusions and future work are finally reported in Section 6.

2. PROBLEM FORMULATION

2.1. Approximate Poisson likelihood

The measured histogram of photon counts $y_{n,t,k}$, for the nth pixel, the tth time bin and the kth wavelength, follows a Pois-

son distribution $\mathcal{P}(.)$ given by [16, 17]:

$$y_{n,t,k} \sim \mathcal{P}(s_{n,t,k}) \qquad (1)$$

where $s_{n,t,k}$ is related to the target's depth d_n and reflectivity $r_{n,k}$ parameters as follows

$$s_{n,t,k} = r_{n,k}f_k(t-d_n) + b_{n,t,k} \qquad (2)$$

with f_k the system impulse response function (IRF), and $b_{n,t,k}$ the background counts due to the environment of observation. In the presence of obscurants, the background might be variable w.r.t. t instead of the commonly used uniform temporal shape. In this paper, instead of considering an accurate likelihood leading to computationally expensive inference, we adopt likelihood approximations and introduce appropriate parameter regularization to recover robust estimates. Assuming: (i) the availability of a background rejection method to extract signal counts ${}^s y_{n,t,k}$ (as introduced in Section 3.6), (ii) a Gaussian shape for the kth IRF with variance σ_k^2 and (iii) that $\sum_{t=1}^T f_k(t-d_n) = 1, \forall k$ for all realistic d_n, straightforward computations lead to the approximate likelihood

$$P({}^s\boldsymbol{Y}_n|\boldsymbol{r}_n,d_n) \quad \propto \quad \prod_{k=1}^K \left[\mathcal{G}(r_{n,k};1+\bar{s}_{n,k},1) \bar{Q}({}^s\boldsymbol{y}_{n,k}) \right]$$
$$\times \quad \mathcal{N}(d_n;d_n^{\mathrm{ML}},\bar{\sigma}^2) \qquad (3)$$

where $\propto$ means "proportional to", $\mathcal{N}(x;\mu,\sigma^2)$ denotes the Gaussian distribution with average μ and variance σ^2, and $\mathcal{G}(x;\gamma,\theta) \propto x^{\gamma-1}\exp(-x/\theta)$ is the gamma distribution with shape and scale parameters γ,θ. In (3), $\bar{Q}({}^s\boldsymbol{y}_{n,k})$ represents a normalization constant depending on the signal counts ${}^s\boldsymbol{y}_{n,k}$ (but not on the parameters of interest $\boldsymbol{r}_n,d_n$), $\bar{s}_{n,k} = \sum_{t=1}^T {}^s y_{n,t,k}$ represents the sum of signal counts per pixel and wavelength, $\bar{\sigma}^2 = \left(\sum_k \frac{\bar{s}_{n,k}}{\sigma_k^2}\right)^{-1}$ and $d_n^{\mathrm{ML}} = \bar{\sigma}^2 \sum_{k=1}^K \frac{\sum_{t=1}^T t\, {}^s y_{n,t,k}}{\sigma_k^2}$ represents the maximum likelihood (ML) depth estimate (i.e., the Gaussian's mean). The joint likelihood for all pixels is

$$P({}^s\boldsymbol{Y}|\boldsymbol{d},\boldsymbol{R}) = \prod_{n=1}^N \prod_{k=1}^K \prod_{t=1}^T P({}^s y_{n,t,k}|r_{n,k},d_n) \qquad (4)$$

after considering independence between the observed pixels $y_{n,t,k}$, and ${}^s\boldsymbol{Y},\boldsymbol{d},\boldsymbol{R}$ are matrices gathering signal counts, depth parameters, and reflectivity parameters, respectively. The ML estimator of the depth and reflectivity parameters is poor especially in challenging scenarios (i.e., sparse photon regime, scattering environment), hence the need for an advanced restoration strategy. Fortunately, (3) highlights the independence of the depth and reflectivity variables, that appear within conventional Gaussian and gamma distributions, which help the design of the proposed Bayesian model.

2.2. Multiscale information

Multiscale information has been widely adopted in several state-of-the-art single-photon restoration algorithms [16, 17, 22, 26, 27]. This strategy improves the robustness of the estimated depth and reflectivity parameters. On the one hand, filtering the histograms of counts with a low-pass uniform filter preserves data Poisson statistics, and leads to estimates with lower noise but with reduced spatial details. On the other hand, the ML estimates are noisy but sharp. In this paper, we combine both information to obtain robust and sharp parameter estimates. Considering L predefined graphs of neighbours $\phi^{1,\cdots,L}$, we compute L downsampled histogram of counts to obtain $\boldsymbol{Y}_k^\ell$ (for example, $\phi^{(2)}$ using $q^{(2)} = 3 \times 3$ neighbours, and $\phi^{(3)}$ using $q^{(3)} = 5 \times 5$ neighbours, $\cdots$). After assuming data independence, the corresponding approximate L likelihood distributions are given by

$$P({}^s\boldsymbol{Y}_n^{(\ell)}|\boldsymbol{r}_n^{(\ell)},d_n^{(\ell)}) \quad \propto \quad \prod_{k=1}^K \left[\mathcal{G}\left(r_{n,k}^{(\ell)};1+\bar{s}_{n,k}^{(\ell)},1\right) \bar{Q}\left({}^s\boldsymbol{y}_{n,k}^{(\ell)}\right) \right]$$
$$\times \quad \mathcal{N}\left(d_n^{(\ell)};d_n^{\mathrm{ML}(\ell)},\left(\bar{\sigma}^{(\ell)}\right)^2\right), \qquad (5)$$

$\forall \ell \in \{1,\cdots,L\}$, with $\ell = 1$ the original cube and $\ell > 1$ are downsampled histograms, and $\left(\bar{\sigma}^{(\ell)}\right)^2 = \left(\sum_k \frac{\bar{s}_{n,k}^{(\ell)}}{\sigma_k^2}\right)^{-1}$.

3. HIERARCHICAL BAYESIAN MODEL

3.1. Prior distribution for depth

Equation (5) indicates L multiscale depth variables $\boldsymbol{d}^{(\ell)}$ having different variances, i.e., different noise levels. Our goal is to generate a single depth map, with smooth object surfaces and well defined object borders. This requires enforcing spatial correlation between the pixels of a surface, while preserving edges of separated surfaces due to isolated objects. This is ensured by connecting a latent variable $\boldsymbol{x}$ (of size $N \times 1$) to the multi-scale depth maps $\boldsymbol{d}^{(\ell)}, \forall \ell$ as follows

$$x_n|d_{\nu_n}^{(1,\cdots,L)},w_{\nu_n,n}^{(1,\cdots,L)},\epsilon_n \sim \prod_{n'\in\nu_n} \left[\prod_{\ell=1}^L \mathcal{L}\left(x_n;d_{n'}^{(\ell)},\frac{\epsilon_n}{w_{n',n}^{(\ell)}}\right) \right] \qquad (6)$$

where $\mathcal{L}(x;\mu,\epsilon) = 1/(2\epsilon)\exp(-|x-\mu|/\epsilon)$ denotes the Laplace distribution where μ,ϵ are the average and diversity parameters, ν_n denotes the nth neighbouring pixels, $\epsilon_n > 0$ is the variance of $\boldsymbol{x}_n$ and $w_{n',n}^{(\ell)} \geq 0$ are fixed weights to be defined. The prior in (6) preserves edges by considering the sparsity promoting ℓ_1-norm of the differences between $\boldsymbol{x}$ and $\boldsymbol{D} = \left[\boldsymbol{d}^{(1)},\cdots,\boldsymbol{d}^{(L)}\right]$. The weights $w_{n',n}^{(\ell)} \geq 0$ connect the variables $\boldsymbol{x}$ and $\boldsymbol{D}$ and can be used to guide these correlations using any available additional information (e.g., by exploiting the results of advanced denoising algorithms as in plug-and-play approaches, or by using other sensors in multi-modal imaging).

3.2. Prior distribution for reflectivity

Similarly to the depth, spatial smoothness is promoted on the reflectivity by considering an $N \times K$ latent variable $\boldsymbol{M}$ following a Gaussian prior distribution given by

$$m_{n,k} | r_{\nu_n,k}^{(1,\cdots,L)}, v_{\nu_n,n}^{(1,\cdots,L)}, \psi_{n,k}^2 \sim \prod_{n' \in \nu_{n,\ell}} \mathcal{N}\left(r_{n',k}^{(\ell)}, \frac{\psi_{n,k}^2}{v_{n',n;k}^{(\ell)}}\right) \quad (7)$$

where $v_{n',n;k}^{(\ell)} \geq 0$ are constant weights, and $\psi_{n,k}^2$ is related to the variance of $\boldsymbol{m}_k$ and will be used to evaluate the reflectivity uncertainty for the kth wavelength. The introduced variable $\boldsymbol{m}_k$ (of size $N \times 1$) contains reflectivity information through its connection to $r_{n,k}^{(\ell)}$ and will be used as the reflectivity estimate for the kth wavelength. Note finally that this prior will provide non-negative analytical estimates for $\boldsymbol{M}, \boldsymbol{R}$.

3.3. Prior distributions for the hyperparameters

The depth and reflectivity variances ϵ_n, and $\psi_{n,k}^2, \forall n, k$ provide a quantitative measure of parameter's uncertainties. These are assigned conjugate inverse gamma distributions

$$f(\boldsymbol{\epsilon}) = \prod_{n=1}^{N} \mathcal{IG}(\epsilon_n; \alpha_d, \beta_d)$$

$$f(\boldsymbol{\Psi}) = \prod_{k=1}^{K} \prod_{n=1}^{N} \mathcal{IG}(\psi_{n,k}^2; \alpha_r, \beta_r) \quad (8)$$

with $\alpha_d, \beta_d, \alpha_r, \beta_r$ denoting positive hyperparameters that are fixed to 0.001 in what follows to obtain a non-informative prior (other values could be used in presence of additional knowledge).

3.4. Posterior distribution

The resulting parameter posterior distribution is given by (after dropping indices for clarity)

$$f(\boldsymbol{x}, \boldsymbol{D}, \boldsymbol{M}, \boldsymbol{R}, \boldsymbol{\epsilon}, \boldsymbol{\Psi} | \boldsymbol{Y}) \propto f(\boldsymbol{Y} | \boldsymbol{R}, \boldsymbol{D}) f(\boldsymbol{D}, \boldsymbol{x} | \boldsymbol{\epsilon}, \boldsymbol{W})$$
$$f(\boldsymbol{R}, \boldsymbol{M} | \boldsymbol{\Psi}, \boldsymbol{V}) f(\boldsymbol{\epsilon}) f(\boldsymbol{\Psi}) \quad (9)$$

where $\boldsymbol{W}$ and $\boldsymbol{V}$ are the depth and reflectivity weights, respectively. Different Bayesian estimators could be used to exploit this posterior. Here we approximate the maximum a posteriori (MAP) estimator for all parameters using a coordinate descent algorithm that iteratively maximizes the posterior distribution with respect to each parameter while fixing the others. The latter updates the parameters iteratively by maximizing their conditional distributions, where $\boldsymbol{x}$ is updated using a weighted median filter [28], $\boldsymbol{D}$ using an analytical generalized soft-threshold operator [29], $\boldsymbol{M}$ using an analytical weighted sum as for the bilateral filter [30], and $\boldsymbol{R}, \boldsymbol{\epsilon}, \boldsymbol{\Psi}$ using efficient analytical expressions. Note finally that the depth related parameters $\boldsymbol{D}, \boldsymbol{x}, \boldsymbol{\epsilon}$ are independent from the reflectivity ones $\boldsymbol{R}, \boldsymbol{M}, \boldsymbol{\Psi}$ allowing their parallel optimization.

3.5. Depth and reflectivity weights: $\boldsymbol{W}, \boldsymbol{V}$

The depth and reflectivity weights control the relation between the multiscale variables $\boldsymbol{D}, \boldsymbol{R}$ and the latent ones $\boldsymbol{x}, \boldsymbol{M}$. In this paper, we assume the presence of a guiding depth $\underline{\boldsymbol{d}}^{(\ell)}, \ell = 1, \cdots, L$ and a guiding reflectivity $\underline{\boldsymbol{r}}_k^{(\ell)}, \forall k, \ell$, obtained using the Lidar data, or as a side information from other sensors (e.g., depth from a radar). The weights can be set to promote similarity to the guides as follows

$$w_{n,n'}^{(\ell)} = w_{\text{norm}} \left[\prod_{\ell'=1}^{\ell-1} \left(1 - w_{n,n'}^{(\ell')}\right)\right] \exp\left(-\frac{|d_n^{\text{ML}(\ell)} - \underline{d}_{n'}^{(\ell)}|}{2\zeta q^{(\ell)}}\right)$$

$$v_{n,n';k}^{(\ell)} = v_{\text{norm}} w_{n,n'}^{(\ell)} \exp\left(-\frac{|r_{n,k}^{\text{ML}(\ell)} - \underline{r}_{n',k}^{(\ell)}|}{2\eta_{n,k} q^{(\ell)}}\right) \quad (10)$$

where w_{norm} (resp., v_{norm}) is a normalization constant ensuring $\sum_{\ell,n'} w_{n,n'}^{(\ell)} = 1$ (resp., $\sum_{\ell,n'} v_{n,n';k}^{(\ell)} = 1$), the coefficients $\zeta, \eta_{n,k}$ are easily fixed based on physical considerations. Here we consider a point-cloud outlier rejection applied to $\boldsymbol{D}$ (i.e., *pcdnoise* in Matlab) to estimate the depth guides $\underline{\boldsymbol{d}}^{(\ell)}, \forall \ell$, and $\underline{\boldsymbol{r}}_k^{(\ell)} = \bar{s}_{n,k}^{\ell}, \forall k, \ell$.

3.6. Background estimation

The proposed method assumes the presence of signal counts without background (which explains the absence of the background in the Bayesian model). Here we present a strategy to unmix signal and non-uniform background. In presence of a spatially homogeneous distribution of the obscurant, the background rate $b_{n,t,k}$ can be assumed smooth. Therefore, low-pass filtered histograms $y_{n,t,k}^{(L)}$ are the sum of a sparse target reflected signal and a smooth function $\hat{b}_{n,t,k}$. The background temporal shape can then be estimated as follows

$$\bar{b}_{t,k} = \text{median}\left(y_{\sqcap_n,t,k}^{(L)}\right) \quad (11)$$

when assuming a fixed shape for all pixels, where $\sqcap_n$ represent the indices of the lowest 10% values of $y_{n,t,k}^{(L)}$ to only consider background and reject signal returns (i.e., assuming that for each time bin at least 10% of pixels only contain background without a target). Each pixel's noise level can be estimated using the median as follows [31]

$$\underline{b}_{n,k} = \text{median}\left(y_{n,:,k}^{(L)}\right) \quad (12)$$

leading to the following background rate estimate and approximate signal counts

$$\hat{b}_{n,t,k} = \max\left(0, \underline{b}_{n,k} + \bar{b}_{t,k} - \bar{\bar{b}}_k\right), \forall t, n,$$

$${}^s y_{n,t,k}^{(\ell)} = \max(y_{n,t,k}^{(\ell)} - \hat{b}_{n,t,k}, 0), \forall n, \text{for } t \in [t_l, t_h] \quad (13)$$

with $\bar{\bar{b}}_k = \sum_t \bar{b}_{t,k}/T$, $t_l = \max(1, d_n^{\text{ML}(\ell)} - I_k^l)$, $t_h = \min(T, d_n^{\text{ML}(\ell)} + I_k^r)$, where I_k^l and I_k^r represent the attack and trailing width of the kth IRF.
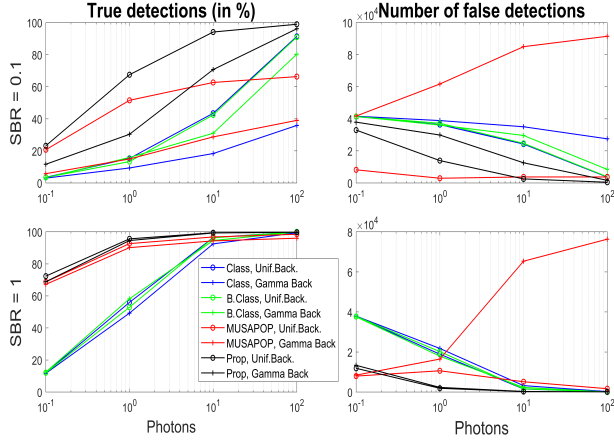
Fig. 1. Comparison of different algorithms based on true and false detections for an error distance of $\tau = 10$bins and different SBR, PPP and background shapes.

4. RESULTS ON SIMULATED DATA

The proposed algorithm is evaluated on simulated multispectral data generated using the cluttered Art scene from the Middlebury dataset[1] [16, 32]. The multispectral data has 283×183 pixels, $T = 300$ bins and $K = 3$ wavelengths. Our algorithm is used with $L = 3$ scales, $q^{(2)} = 3 \times 3$, $q^{(3)} = 9 \times 9$ which could be used as default values for other scenes, and $\zeta = 2.7$cm which is related to the IRF width and depth resolution. Note that larger scales could be used when processing extremely noisy data. The algorithm is compared to: (i) Class. which is the Classical matched filter assuming no background, (ii) B-Class.: which first removes background using the proposed method in Section 3.6 and then apply Class., (iii) the state-of-the-art multispectral algorithm MUSAPOP [14]. We simulate two levels of signal-to-background ratio SBR$\in \{0.1, 1\}$, vary the full average photons-per-pixel (PPP) in $[0.1, 100]$, and consider uniform-shaped and gamma-shaped background noise (gamma distribution with parameters $\alpha = 2$ and $\beta = 30$) [9]). Fig. 1 shows the obtained detection probablities (see [14]) where a point is considered true if there is a ground-truth point within $\tau = 10$bins. B-Class outperforms Class. indicating the benefit of the proposed background estimation step. The proposed method presents higher true detection probabilities and lower false detections compared to MUSAPOP, especially in presence of non-uniform background. These results highlight the robustness of the proposed method.

5. RESULTS ON REAL DATA

We also consider the use of challenging real data provided by [18]. We focus on the elephant scene which has 256×256 pixels, $T = 1536$ time bins and $K = 1$ wavelength, an
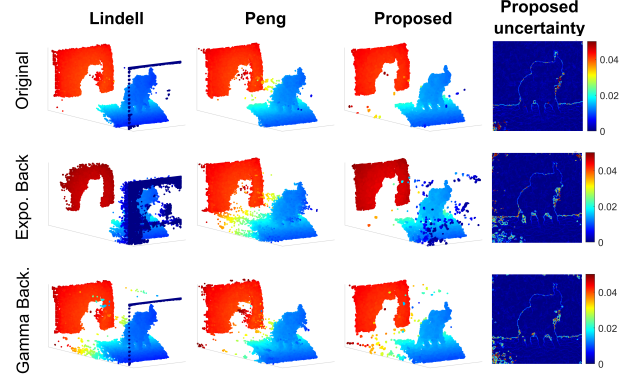

Fig. 2. Results on the elephant scene. (Top row) original data, (middle) exponential shaped background, (bottom) gamma shape background. Uncertainty or depth variance is ϵ in cm.

average total PPP of 2.5, and SBR ≈ 0.5. To highlight the robustness of the proposed algorithm to background's shapes, we add to the original elephant histograms Poisson's distributed background counts with different temporal shapes: exponential decreasing (as observed in [12]), or gamma (as in [9]). For each pixel, the exponential shape is generated using $800/N\exp(-0.005t)$ (resp. gamma shape using $0.2t^{1.5}\exp(-0.005t)$), leading to an additional 2.5 background photon per pixel on average. Our algorithm is used with $L = 4$, $q^{(2)} = 3^2$, $q^{(3)} = 19^2$, $q^{(4)} = 21^2$, $\zeta = 3.5$cm and is compared to Lindell's [18] and Peng's [20] algorithms. Both [18] and [20] output depth maps, thus we will only consider the depth estimates of our algorithm in this evaluation. Fig. 2 shows the obtained depth results. All algorithms perform similarly when considering the original data with some outliers around the elephant mouth. Adding more background highlights the robustness of the proposed model to different shapes since it shows less outliers. The method also provides uncertainty maps presenting higher values in noisy regions. These maps can also be used to localise high uncertainty estimates and help decision making. In all these results, the proposed algorithm converged rapidly in approximately 3 or 4 iterations.

6. CONCLUSIONS

This paper presents a Bayesian strategy for the robust reconstruction of multispectral single-photon data when imaging through obscurants. The method provides depth and reflectivity estimates with quantified uncertainty to help with decision making. It also exploits data's multiscale information to improve robustness, and can incorporate guide information coming from other imaging sensors or by considering off-the-shelf denoisers. Validation on simulated and real data shows best results in comparison to other algorithms, in presence of a high and non-uniform background noise. Future work will consider the acceleration of the current Matlab code using parallel computing tools (such as GPUs).

---

[1] Available in: http://vision.middlebury.edu/stereo/data/

7. REFERENCES

[1] A. M. Wallace, A. Halimi, and G. S. Buller, "Full waveform lidar for adverse weather conditions," *IEEE Trans. Vehicular Tech.*, vol. 69, no. 7, pp. 7064–7077, 2020.

[2] J. Rapp, J. Tachella, Y. Altmann, S. McLaughlin, and V. K. Goyal, "Advances in single-photon lidar for autonomous vehicles: Working principles, challenges, and recent advances," *IEEE Signal Processing Magazine*, vol. 37, no. 4, pp. 62–71, 2020.

[3] A. Kirmani, D. Venkatraman, D. Shin, A. Colaço, F. N. C. Wong, J. H. Shapiro, and V. K. Goyal, "First-photon imaging," *Science*, vol. 343, no. 6166, pp. 58–61, 2014.

[4] D. Shin, A. Kirmani, V. K. Goyal, and J. H. Shapiro, "Photon-efficient computational 3-d and reflectivity imaging with single-photon detectors," *IEEE Transactions on Computational Imaging*, vol. 1, no. 2, pp. 112–125, 2015.

[5] A. M. Pawlikowska, A. Halimi, R. A. Lamb, and G. S. Buller, "Single-photon three-dimensional imaging at up to 10 kilometers range," *Opt. Express*, vol. 25, no. 10, pp. 11 919–11 931, May 2017.

[6] Z.-P. Li, X. Huang, Y. Cao, B. Wang, Y.-H. Li, W. Jin, C. Yu, J. Zhang, Q. Zhang, C.-Z. Peng, F. Xu, and J.-W. Pan, "Single-photon computational 3D imaging at 45 km," *Photon. Res.*, vol. 8, no. 9, pp. 1532–1540, Sep 2020.

[7] Z.-P. Li, J.-T. Ye, X. Huang, P.-Y. Jiang, Y. Cao, Y. Hong, C. Yu, J. Zhang, Q. Zhang, C.-Z. Peng, F. Xu, and J.-W. Pan, "Single-photon imaging over 200km," *Optica*, vol. 8, no. 3, pp. 344–349, Mar 2021.

[8] A. Maccarone, F. M. D. Rocca, A. McCarthy, R. Henderson, and G. S. Buller, "Three-dimensional imaging of stationary and moving targets in turbid underwater environments using a single-photon detector array," *Opt. Express*, vol. 27, no. 20, pp. 28 437–28 456, Sep 2019.

[9] G. Satat, M. Tancik, and R. Raskar, "Towards photography through realistic fog," in *Computational Photography (ICCP), 2018 IEEE International Conference on*. IEEE, 2018, pp. 1–10.

[10] R. Tobin, A. Halimi, A. McCarthy, M. Laurenzis, F. Christnacher, and G. S. Buller, "Three-dimensional single-photon imaging through obscurants," *Opt. Express*, vol. 27, no. 4, pp. 4590–4611, Feb 2019.

[11] A. Halimi, A. Maccarone, R. A. Lamb, G. S. Buller, and S. McLaughlin, "Robust and guided bayesian reconstruction of single-photon 3D lidar data: Application to multispectral and underwater imaging," *IEEE Trans. Comput. Imaging*, vol. 7, pp. 961–974, 2021.

[12] R. Tobin, A. Halimi, A. McCarthy, P. Soan, and G. S. Buller, "Robust real-time 3D imaging of moving scenes through atmospheric obscurant using single-photon LiDAR," *Scientific Reports*, vol. 11, p. 11236, 2021.

[13] S. Hernandez-Marin, A. M. Wallace, and G. J. Gibson, "Multilayered 3D lidar image construction using spatial models in a bayesian framework," *IEEE Trans. Pattern Anal. Mach. Intell.*, vol. 30, no. 6, pp. 1028–1040, June 2008.

[14] J. Tachella, Y. Altmann, M. Márquez, H. Arguello-Fuentes, J. Y. Tourneret, and S. McLaughlin, "Bayesian 3D reconstruction of subsampled multispectral single-photon lidar signals," *IEEE Trans. Comput. Imaging*, vol. 6, pp. 208–220, 2020.

[15] A. Halimi, A. Maccarone, A. McCarthy, S. McLaughlin, and G. S. Buller, "Object depth profile and reflectivity restoration from sparse single-photon data acquired in underwater environments," *IEEE Trans. Comput. Imaging*, vol. 3, no. 3, pp. 472–484, 2017.

[16] J. Rapp and V. K. Goyal, "A few photons among many: Unmixing signal and noise for photon-efficient active imaging," *IEEE Trans. Comput. Imaging*, vol. 3, no. 3, pp. 445–459, Sept. 2017.

[17] A. Halimi, R. Tobin, A. McCarthy, J. Bioucas-Dias, S. McLaughlin, and G. S. Buller, "Robust restoration of sparse multidimensional single-photon lidar images," *IEEE Trans. Comput. Imaging*, vol. 6, pp. 138–152, 2020.

[18] D. B. Lindell, M. O'Toole, and G. Wetzstein, "Single-photon 3D imaging with deep sensor fusion," *ACM Trans. Graph.*, vol. 37, no. 4, pp. 113:1–113:12, July 2018.

[19] Z. Sun, D. B. Lindell, O. Solgaard, and G. Wetzstein, "Spadnet: deep rgb-spad sensor fusion assisted by monocular depth estimation," *Opt. Express*, vol. 28, no. 10, pp. 14 948–14 962, May 2020.

[20] J. Peng, Z. Xiong, X. Huang, Z.-P. Li, D. Liu, and F. Xu, "Photon-efficient 3D imaging with a non-local neural network," in *Computer Vision – ECCV 2020*. Cham: Springer International Publishing, 2020, pp. 225–241.

[21] A. Ruget, S. McLaughlin, R. K. Henderson, I. Gyongy, A. Halimi, and J. Leach, "Robust super-resolution depth imaging via a multi-feature fusion deep network," *Opt. Express*, in press.

[22] W. Marais and R. Willett, "Proximal-gradient methods for poisson image reconstruction with BM3D-based regularization," in *2017 IEEE 7th International Workshop on Computational Advances in Multi-Sensor Adaptive Processing (CAMSAP)*, 2017, pp. 183–187.

[23] J. Tachella, Y. Altmann, N. Mellado, A. McCarthy, R. Tobin, G. S. Buller, J.-Y. Tourneret, and S. J. McLaughlin, "Real-time 3D reconstruction from single-photon lidar data using plug-and-play point cloud denoisers," *Nature Communications*, vol. 10, no. 1, p. 4984, 2019.

[24] Y. Romano, M. Elad, and P. Milanfar, "The little engine that could: Regularization by denoising (red)," *SIAM Journal on Imaging Sciences*, vol. 10, no. 4, pp. 1804–1844, 2017.

[25] Y. L. V. Monga and Y. C. Eldar, "Algorithm unrolling: Interpretable, efficient deep learning for signal and image processing," *IEEE Signal Processing Magazine.*, 2020, to appear.

[26] J. Tachella, Y. Altmann, X. Ren, A. McCarthy, G. S. Buller, S. McLaughlin, and J.-Y. Tourneret, "Bayesian 3D reconstruction of complex scenes from single-photon lidar data," *SIAM Journal on Imaging Sciences*, vol. 12, no. 1, pp. 521–550, 2019.

[27] S. Chen, A. Halimi, X. Ren, A. McCarthy, X. Su, S. McLaughlin, and G. S. Buller, "Learning non-local spatial correlations to restore sparse 3D single-photon data," *IEEE Trans. Image Process.*, vol. 29, pp. 3119–3131, 2020.

[28] Q. Zhang, L. Xu, and J. Jia, "100+ times faster weighted median filter (wmf)," in *2014 IEEE Conference on Computer Vision and Pattern Recognition*, June 2014, pp. 2830–2837.

[29] R. Nassif, C. Richard, A. Ferrari, and A. H. Sayed, "Proximal multitask learning over networks with sparsity-inducing coregularization," *IEEE Trans. Signal Process.*, vol. 64, no. 23, pp. 6329–6344, 2016.

[30] C. Tomasi and R. Manduchi, "Bilateral filtering for gray and color images," in *Sixth International Conference on Computer Vision (IEEE Cat. No.98CH36271)*, 1998, pp. 839–846.

[31] I. Gyongy, S. W. Hutchings, A. Halimi, M. Tyler, S. Chan, F. Zhu, S. McLaughlin, R. K. Henderson, and J. Leach, "High-speed 3D sensing via hybrid-mode imaging and guided upsampling," *Optica*, vol. 7, no. 10, pp. 1253–1260, Oct 2020.

[32] D. Scharstein and C. Pal, "Learning conditional random fields for stereo," in *2007 IEEE Conference on Computer Vision and Pattern Recognition*, June 2007, pp. 1–8.